TESTING THE GLOBAL STAR FORMATION RELATION:

AN HCO^+ (3-2) MAPPING STUDY OF RED MSX SOURCES IN THE BOLOCAM GALACTIC PLANE SURVEY

By

DAVID ERIC SCHENCK

A Thesis Submitted to the Honors College

In Partial Fulfillment of the Bachelors Degree

With Honors in

Astronomy

THE UNIVERSITY OF ARIZONA

MAY 2011

Approved by:

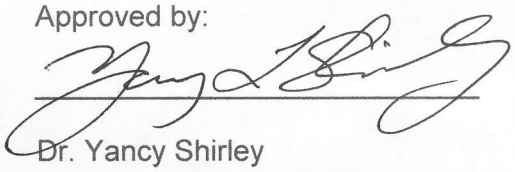

Dr. Yancy Shirley

Steward Observatory

Testing the global star formation relation: An HCO^+ (3-2) mapping study of Red MSX sources in the Bolocam Galactic Plane Survey

David E. Schenck[1,2] , Yancy L. Shirley[1,3], Megan Reiter[1],

and

Stephanie Juneau[1]

1. Abstract

We present an analysis of the relation between the star formation rate (SFR) and mass of dense gas in Galactic clumps and galaxies. Using the bolometric luminosity as a measure of SFR and the molecular line luminosity of HCO^+ (3-2) as a measure of gas mass, we find that the relation between SFR and M_{dense} is approximately linear. This is similar to the results in Gao and Solomon (2004a,b) and Wu et al. (2010) derived using HCN (1-0) as the dense gas tracer. Our work includes 16 Galactic clumps that are in both the Bolocam Galactic Plane Survey and the Red MSX Survey, 27 water maser sources from Reiter et al. (2011), and the aforementioned HCN (1-0) data. Our results agree qualitatively with the predictions of Krumholz and Thompson (2007) and Narayanan et al. (2008) which state that the nature of the relation should depend on how the critical density of the tracer compares with the mean density of the gas.

2. Introduction

All stars originate in clouds of cold, dense molecular gas (Evans 1999). The formation of low-mass stars is well studied and the process by which it occurs is understood (Shu, Adams, & Lizano 1987, André et al. 2000). However, the formation of stars with masses greater than $\sim$8 $M_\odot$ is more difficult to examine because the regions in which they form are considerably farther away (Wu et al. 2010). High-mass stars may not simply be a scaled-up

[1]Steward Observatory, University of Arizona, 933 Cherry Ave., Tucson, AZ 85721

[2]Honors Thesis

[3]Adjunct Astronomer at the National Radio Astronomy Observatory

version of low-mass stars, but instead may be formed in a fundamentally different way (e.g., competitive accretion, clump coalescence vs. scaled-up accretion; see McKee & Ostriker 2007). A complete theory of star formation requires an understanding of the efficiency and rate of forming stars across the entire stellar mass range.

In the last few years, a new nomenclature has been adopted to describe the structure of Galactic star-forming regions within molecular clouds. Protostars form from individual dense cores of gas. Most protostars form in clustered environments and collections of cores which may be physically connected or gravitationally bound within a larger clump. Clumps located in the Milky Way are near enough to be observed in detail using submillimeter single-dish telescopes with resolutions of tens of arcseconds (e.g., Reiter et al. 2011). The information gained from studies of these local star-forming clumps can be used to understand star formation in galaxies too far away to resolve individual star-forming regions. Ultimately, these studies may be used to constrain a universal star formation law.

Determining the rate and efficiency of star formation has been a long standing problem. It was first proposed by Schmidt in 1959 that the rate of star formation would depend on the volume density of dense gas according to a power law. Building upon this assumption, it was shown globally for galaxies that the power law phrased in terms of surface density gave $\Sigma_{SFR} \propto \Sigma_{gas}^{1.4\pm0.15}$ (Kennicutt 1998). This relation, which was derived using CO to trace the molecular gas and HI to trace the atomic gas is called the Kennicutt-Schmidt relation (K-S relation). Even with the resolution of state-of-the-art interferometers, the K-S relation has only been probed down to scales of ≈ 1 kpc, much larger than the sizes of giant molecular clouds (tens of pc) in nearby galaxies (e.g., Bigiel et al. 2011). The K-S relation has been questioned because CO observations probe low density molecular emission and not the dense molecular gas more directly associated with the clumps and cores from which protostars form (e.g. Gao & Solomon 2004a). Therefore, subsequent studies have tested the power law relation by measuring the molecular line luminosity of tracers that specifically trace the dense gas mass. Using the line luminosity of the transition HCN (1-0) and infrared luminosity of a set of 65 galaxies, including LIRGs and ULIRGs, Gao & Solomon (2004a,b) found a power law index of 1.00 ± 0.05. They interpreted this result as the SFR being proportional to dense gas mass (Gao & Solomon 2004a,b). This HCN (1-0) survey was extended to the scale of Galactic dense cores with similar results; the power law index was very near one over a range of 7 orders of magnitude in L_{IR} (Wu et al. 2005, Wu et al. 2010). This was interpreted as evidence that there is a fundamental unit of star formation associated with massive clumps with luminosities $L_{bol} > 10^{4.5} L_{\odot}$ and the star formation efficency within the dense clumps is constant.

Since the initial work of Gao & Solomon and Wu et al., a wider range critical densities

has been probed by molecular tracer (e.g. Bussmann et al. 2008, Juneau et al. 2009). Theoretical radiative transfer models predict the behavior of the SFR and line luminosity on gas density on galactic scales (Krumholz and Thompson 2007, Narayanan et al. 2008). The behavior of the line luminosity is dependent on the critical density of the tracer in their models; if the critical density exceeds the mean density, the line luminosity rises superlinearly with density. However, for critical densities below the mean density, it rises linearly. The SFR is assumed to rise superlinearly with density in these models, similar to the original Schmidt relation (1959) but different from the conclusion of Gao & Solomon. Combining the two conditions gives high critical density tracers linear correlations and low critical density tracers superlinear correlations. This general trend is observed in galaxies using CO (1-0), HCN (1-0) and (3-2), and HCO^+ (1-0) and (3-2) (Juneau et al. 2009).

The results of Gao and Solomon (2004) and Wu et al. (2010) provide evidence that the SFR to dense gas mass ratio is constant. However, the extragalactic community and many theoretical models continue to assume a superlinear Schmidt relation. In this paper, we test the observed Gao & Solomon and Wu et al. correlation, by mapping a sample of 16 massive cores in HCO^+ (3-2) selected from the Bolocam Galactic Plane Survey (Aguirre et al. 2011). This sample is combined with 27 massive clumps mapped in HCO^+ (3-2) that are associated with water masers from Reiter et al. (2011) and 14 (U)LIRGs, from Juneau et al. (2009) that were adapted from Graciá-Carpio et al. (2008) using updated distances. We also conduct a re-analysis of the 50 dense clumps from Wu et al. (2010) and 42 galaxies from Gao and Solomon (2004) to verify the published HCN correlation.

We choose HCO^+ (3-2) because of its ability to trace nearly identical excitation conditions to HCN (1-0). The frequency and dipole moment of HCO^+ (3-2) are a factor of $\sim$3 and $\sim$1.5 times higher than the corresponding values of HCN (1-0). The Einstein A coefficient is proportional to $\nu^3\mu^2$, making the Einstein A coefficient of HCO^+ (3-2) $\sim$ 60 times higher. Most of this disparity is compensated by HCO^+ inducing dipoles in the molecules with which it interacts, increasing the effective cross section for collision and the corresponding collision rate γ_{jk}. HCN is not an ion, so it does not induce a dipole in nearby molecules and it has a comparatively lower rate of de-excitation. At 20 K, HCO^+ (3-2) and HCN (1-0) have critical densities of 3.90×10^6 and 1.25×10^6 cm^{-3}, respectively, a factor of $\sim$3.1 difference. Since the excitation of a molecular line varies gradually over a range of densities, claiming the line traces gas at the critical density is an oversimplification (Evans 1999). A more practical quantity is the effective density for excitation, n_{eff}, which is defined as the density at which a transition will have a radiation temperature of 1 K assuming log(N/Δv)=13.5 cm^{-2}/km/s and an average kinetic temperature of 20 K (see Reiter et al. 2011). The two transitions also have even more similar effective densities; HCO^+ (3-2) and HCN (1-0) have effective densities of 2.33×10^4 and 1.50×10^4 cm^{-3}. These only differ by a factor of $\sim$1.5. Densities

can range over several magnitudes within molecular clouds, so such a small difference means the transitions essentially trace the same molecular gas in the absence of strong chemical differentiation.

In §2, we summarize the observations of our sample of 16 massive cores as well as the full (combined) sample used in this paper. In §3, we discuss the methods used to derive physical quantities from the maps. We present our results and compare them to both other observations and theoretical predictions in §4 as well as critically discuss several caveats with the interpretation of the observed correlation.

3. Observations

Sixteen sources were mapped using the 10-meter Heinrich Hertz Telescope (HHT) on Mount Graham, Arizona. Observations were made on April 10 and 11 as well as May 4 through May 9, 2010, excluding May 5. The HHT was equipped with the 1mm ALMA prototype sideband-separating receiver. The observations were made with a 6.0 GHz IF in dual polarization 4 IF mode with the vertical and horizontal polarizations each split into upper and lower sidebands. Two transitions were observed simultaneously; HCO^+ J = 3 → 2 (267.558 GHz) was centered in the lower sideband while N_2H^+ J = 3 → 2 (279.512 GHz) was centered in the upper sideband. The N_2H^+ maps are not included in this analysis because of the weakness of the detections. The observed line properties are listed in Tables 2 and 3. The backend filter-banks were split into 256 channels with 250 kHz resolution. At the frequencies used, the velocity resolution was ∼0.28 km s^{-1}. The maps have an angular resolution of 27.2″.

Maps were made by repeatedly scanning in both RA and DEC. Scan rows were separated by about 10″, about one-third of the beam size. Each source was scanned at least once in the RA and DEC directions and many were scanned again in both. Additional pairs of scans were offset by about 5″ from the first pair to better sample the source. The pointing accuracy of the HHT is typically 5″ RMS.

The maps were reduced using the GILDAS CLASS software. First, a linear baseline was removed from each map. The vertical and horizontal polarizations were scaled separately using their respective main beam efficiencies and then combined (η_H=0.70±0.04, η_V=0.81±0.04). The maps were convolved using a Gaussian-tapered Bessel function of the form $\frac{J_1(\frac{r}{a})}{(\frac{r}{a})} exp[-(\frac{r}{b})^2]$ where a = $1.55(\frac{\theta_{mb}}{3})$ and b = $2.52(\frac{\theta_{mb}}{3})$ (Mangum et al. 2007, Reiter et al. 2011) to preserve spatial resolution.

3.1. Source Selection

The sixteen sources mapped for this project were selected from the BOLOCAM Galactic Plane Survey (BGPS). A total of 1402 BGPS sources spectroscopically observed by Schlingman et al. (2011) were examined by eye using GLIMPSE (8 μm) and MIPSGAL (24 μm) images. The MIPSGAL images were used to determine which sources were associated with a 24 μm point source. The point sources indicate the presence of either an embedded protostar or an evolved star. Each BGPS source within 15″ of the point source was considered to contain a candidate embedded object. The 247 objects associated with 24 μm point sources were then compared to the Red MSX Source (RMS) survey by calculating the offset between their positions. The RMS survey includes over one thousand massive young stellar objects (MYSOs) which are radio-quiet mid-infrared point sources (Mottram et al. 2010). Comparing the coordinates of the objects in each catalogue, 79 from MSX were within 15″ of a BGPS source. Candidate RMS in the BGPS were observed generally in order of brightest to dimmest HCO^+ (3-2) intensity. Not every object common to the two surveys was observed due to observational constraints, but every joint object with I_{HCO^+}(3-2) $>$ 10.5 K km s^{-1} was mapped.

In addition to our observations, we include HCO^+ (3-2) maps from the survey of Reiter et al. (2011). Twenty-seven massive clumps associated with H_2O masers were taken from this paper. Also, fourteen luminous and ultraluminous infrared galaxies (LIRGs and ULIRGs) originally from Graciá-Carpio et al. 2008 represent the currently known extrgalactic observations of HCO^+ (3-2) (Juneau et al. 2009). We analyze the correlation between bolometric luminosity and molecular luminosity for this combined sample using a new Bayesian linear regression technique (Kelly 2007). We also re-analyze the Wu et al. (2004) correlation of 50 massive, dense clumps and 42 galaxies that were mapped in HCN (1-0)(Wu et al. 2010, Gao and Solomon 2004a,b) using the same Bayesian linear regression technique (Kelly 2007). Galaxies which had upper or lower limits on the molecular line luminosity were not used in our analysis.

4. Clump Physical properties

The maps in integrated intensity of HCO^+ (3-2) emission are shown in in Figure 1. Intensities were found from the peak line in each map,

$$I(T_{mb}) = \int T_{mb} dv \pm \sqrt{\delta v_{line} \delta v_{chan}} \sigma_{T_{mb}} \quad (1)$$

where δv_{line} is the velocity extent of the line, δv_{chan} is the channel width of the spectrometer (0.28 km s^{-1}), and $\sigma_{T_{mb}}$ is the uncertainty in the main-beam temperature. The quantity

δv_{line} was derived from setting boundaries on each side of the line so that the entire line was enclosed. As a result, the intensity uncertainty is a conservative estimate. The total sample of galactic cores mapped in HCO^+ (3-2) had a mean intensity of 52.56 ± 50.18 K km^{-1} and a median of 36.48. The mean and median for the subset of BGPS/RMS selected cores are 13.63 ± 9.51 K km^{-1} and 11.69 K km^{-1}. The mean and median for the subset of water maser selected sources are 75.64 ± 50.29 K km^{-1} and 61.48 K km^{-1}. The BGPS selected subset extends the sample of Galactic sources to lower integrated intensities in HCO^+ (3-2).

The angular diameter was defined by the half-peak intensity contour of maps of the molecular eemission and is determined by using the area enclosed within the contour ($\theta_{s*b} = \sqrt{4A/\pi}$). The uncertainty in the half-peak diameter was determined by finding the diameters associated with the half-peak contour $\pm\ \sigma_{T_{mb}}$. The beam of the telescope ($27.2''$) contributed to the width of the maps. This effect was removed by calculating the deconvolved sizes using

$$\theta_{dec} = \sqrt{\theta_{s*b}^2 - \theta_{beam}^2} \tag{2}$$

The distance and angular diameter were used to calculate a physical radius from

$$R = \frac{\theta_{dec} D}{2} \tag{3}$$

where R is the radius in the units of the distance, D, and θ_{dec} is the deconvolved angular diameter in radians. The total sample has a mean size 0.31 ± 0.18 pc and a median of 0.28 pc. The means of the BGPS/RMS and water maser samples are 0.35 ± 0.19 and 0.29 ± 0.16 pc and medians 0.34 and 0.24 pc, respectively. The BGPS/RMS mean is skewed upward by a large source (019.884-053) which is also the brightest in that sample. A histogram of the sizes is presented in Figure 3 along with histograms of other physical properties.

Distances were obtained by using radial velocity measurements to get kinematic distances (Schlingman et al. 2011). Kinematic distances are ambiguous in that two different distances correspond to the same radial velocity in the first quadrant of the Galaxy. Four sources were assigned to the near distance because the appear to be associated with an IRDC. The remaining distances were determined using information supplied by the RMS online catalog (Urquhart et al. 2008) which not only gave kinematic distances, but also a "complex distance." The complex distance was for any MYSOs belonging to a complex with a previously determined distance. If the one of the two kinematic distances was within about 1 kpc of the quoted complex distance, that kinematic distance was assigned. The water maser clumps from Reiter et al. (2011) used distances that were previously determined (see Shirley et al. 2003).

The uncertainty in the distances is needed to propagate the uncertainty in the molecular line luminosity. The uncertainty was determined using distance probability curves produced

by Bower et al. (in prep.). This method employs radial velocity measurements, proximity to IRDCs, H I self-absorption, and other factors to calculate a joint probability distribution (P(D)). The distance probability curves are typically bi-modal (centered on the near and far distance). Each mode of the probabiity curves were fit by Gaussians, one for the near distance and one for the far distance, to determine the spread of the curves. Probability curves were available for all of the BGPS/RMS crossover sources, but only 8 of the 27 water maser sources (Bower, private communication 2010). The remaining 19 sources without distance probability curves were assigned the average uncertainty of those 8. There was no trend between distance and distance uncertainty.

The bolometric luminosities were calculated using the observed spectral energy distribution (SED) of each source. SEDs were constructed uniformly from fluxes taken from the BGPS (1.1 mm), MSX (8, 12, 14, and 21 μm), SCUBA (850 μm), MIPSGAL (70 μm), IRAS (12, 25, 60, and 100 μm), and AKARI (65, 90, 140, and 160 μm). Bolometric luminosities were calculated by integrating over the observed fluxes. Luminosities were already available for the water maser sources, but they were re-calculated because new fluxes had become available since the published SEDs in Mueller et al. (2002). See Table 4 for the complete SEDs of the sources. The mean luminosity of the sample is $10^{5.09\pm0.87}$ $L_\odot$ with a median of $10^{4.52}$ $L_\odot$. The mean bolometric luminosity of the water-maser sources exceeds that of the BGPS/RMS sources; the former is $10^{5.23\pm0.76}$ $L_\odot$ and the latter $10^{4.64\pm0.66}$ $L_\odot$.

L', or the molecular line luminosity, is a commonly used quantity in extragalactic studies as an analogue to the molecular mass. Formally, molecular line luminosity, or source-integrated surface brightness as it is called in Mangum et al. 2008, is defined as

$$L' = 23.504\pi\theta^2_{s*b}(1+z)^{-3}D_L^2 I(T_{mb}) \tag{4}$$

where θ^2_{s*b} is the convolved angular diameter in arcseconds, z is the redshift, D_L is the luminosity distance in Mpc, and $I(T_{mb})$ is the integrated intensity in K km s^{-1}. Two sources with the same main beam brightness temperature and spatial extent will have the same L$'$. The means line luminosity of the BGPS/RMS and water-maser samples were each 33.5 K km s^{-1}. Histograms of the bolometric and line luminosities are shown in Figure 3. In §4.1 we construct the correlation between bolometric luminosity and molecular line luminosity with distance uncertainties propagated for the Galactic sources.

Finally, we calculated the mass in the Galactic clumps using two different methods. Virial masses were calculated using

$$M_{vir} = \frac{5R(\Delta v)^2}{8a_1a_2Gln(2)} \approx \frac{209R(\Delta v)^2}{a_1a_2} \tag{5}$$

$$a_1 = \frac{1-p/3}{1-2p/5} \tag{6}$$

where R is the physical radius in pc, Δv is the FWHM linewidth in km s^{-1}, and a_1 and a_2 are factors that account for a power law density distribution (n $\propto r^{-p}$) and non-spherical shape, respectively (Bertoldi and McKee 1992). The median value of p (1.75), the exponent of the density power law, was adopted from Mueller et al. (2002), making a_1=1.39. The correction factor a_2 is negligible for aspect ratios below 2, so it was set to 1 for all calculations. The linewidth is a measure of the thermal and turbulent support against gravitational collapse, but can be broadened by optically thick emission, leading to overestimates of the virial mass (Shirley et al. 2008, Reiter et al. 2011). The mean virial mass is $10^{3.30\pm0.41}$ M$_\odot$ and a median of $10^{3.13}$ M$_\odot$. For the BGPS/RMS and water-maser samples, the mean is $10^{3.24\pm0.41}$ M$_\odot$ and $10^{3.33\pm0.41}$ M$_\odot$, respectively.

Masses were also estimated from the 1.1 mm continuum emission by assuming a single dust temperature and common dust opacity for all sources. The isothermal mass is

$$M_{iso} = \frac{S_\nu D^2}{B_\nu(T)\kappa_\nu} \tag{7}$$

where S$_\nu$ is the total integrated flux at 1.1 mm and κ_ν is the opacity of that wavelength. The value $\kappa_{1.1mm}$=0.0114 cm^2 g^{-1} was adopted (Ossenkopf & Henning 1994, Battersby et al. 2010, Enoch et al. 2006). This is consistent with a dust-to-mass ratio of 100. Assuming a temperature of 15 K, the equation for M$_{iso}$ becomes

$$M_{iso} = 14.32(e^{13/T} - 1)(\frac{S_\nu}{1Jy})(\frac{D}{1kpc})^2 \mathrm{M}_\odot. \tag{8}$$

The mean isothermal mass is $10^{3.37\pm0.64}$ M$_\odot$. This is higher than the mean for the virial mass. The water-maser sample also has a higher mean isothermal mass ($10^{3.54\pm0.51}$ M$_\odot$), but the mean isothermal mass is lower than the mean virial mass for the BGPS/RMS sources ($10^{3.09\pm0.87}$ M$_\odot$).

5. Results and discussion

A Bayesian linear regression routine written by Brandon Kelly was used to test the correlation between L$'$ and L_{bol} as well as L$'$ and M_{vir}. The program uses a Markov chain Monte Carlo (MCMC) method to take random draws of the slope, intercept, and intrinsic scatter by perturbing the previous set of line parameters. These new sets of parameters are either accepted or rejected according to the Metropolis-Hastings algorithm (Metropolis et al. 1953, Hastings et al. 1970). The program tests 10,000 sets of parameters and saves the distribution of accepted values. The spread in the distribution is of the slopes is entirely attributable to the uncertainties in the data; the uncertainty from the MCMC sampler is

negligible (Brandon Kelly, private communication). For a more detailed description of the program, see Kelly (2007).

The results of the Bayesian fits are presented in Table 5. The lines take the form

$$log(y) = blog(x) + a. \tag{9}$$

The ordinate and absicca variables are listed in Table 5 in the order y-x. The quantity σ_{int} is the intrinsic scatter of the fit.

5.1. M-L′ correlation

First we test the correlation between mass and line luminosity. The mass of Galactic clumps were found using both isothermal mass (determined from dust continuum emission) and virial mass (determied from HCO^+ emission). The M_{iso}-L′ relation had a sublinear slope (0.78 ± 0.10) and the M_{vir}-L′ relation had a linear slope (1.06 ± 0.18). Using M_{iso} produced a slightly tighter correlation; the correlation coefficient for M_{iso} was 0.85 compared to only 0.70 for M_{vir}. The same trends were observed in multiple molecular species in Reiter et al. (2010) and Wu et al. (2010) using the water maser sources.

The virial mass depends on the linewidth, Δv. The line can be artificially broadened if the emission is optically thick which is true for the transitions considered (see Phillips 1979). This effect will cause the virial mass to be an overestimate. Thus, we prefer M_{iso} as an estimate of the clump mass. Nevertheless, our tight linear correlation indicates that L' is indeed a good tracer of the dense gas in clumps.

5.2. L′-L_{bol} correlation

Correlations were found for several subsets of the data by using L′ as the independent variable and L_{bol} as the dependent variable. The slope of the galactic clumps and combined data sets observed in HCO^+ (3-2) both came out to nearly one (1.10 ± 0.12 and 1.04 ± 0.02 respectively). The histograms in the bottom right corner of Figure 2 show the distribution of slopes for the galactic and extragalactic data. The slope for all clumps and galaxies together has an uncertainty nearly a factor of 10 lower than the clumps alone. This is the result of the data appearing in two widely separated groups in L_{bol}-L′ space so that the line was basically fit to two clumps of points. The slope of the correlation for Galactic clumps agrees very well with the Wu et al. (2010) correlation for HCN (1-0) (also see below). While the best-fit line for the Galactic clumps extends to be slightly higher than the extragalactic objects, the

uncertainty on the slope make it such that the extragalactic points are within 1σ of the fit. The extrapolation of the best-fit of the extragalactic points misses the Galactic points more dramatically, although the large uncertainty on the slope still cannot rule out a linear slope at the more than 1σ level. This result is different than was found for HCN (1-0) by Wu et al. (2004; also see below); however, we must caution that the published extragalactic HCO^+ (3-2) detections are small in number and limited to $L_{bol} > 10^{11}$ $L_\odot$. Global extragalactic observations of L′ HCO^+ (3-2) are needed, especially for galaxies with $L_{bol} < 10^{11}$ $L_\odot$ to better compare with the HCN (1-0) results.

Linear fits for the HCN (1-0) data set were presented in Gao and Solomon (2004a,b) and Wu et al. (2010), both of which found a linear relation between L_{IR} and L′. We test their results by re-analyzing their data with the Bayesian routine. The fit displayed in the top right plot of Figure 2 do not include any points below $L_{IR}=10^3$ $L_\odot$. This cutoff was established because that is roughly the lowest L_{bol} in the HCO^+ data set. The limit makes the HCN (1-0) and HCO^+ correlations span the same range in luminosity. The slopes for the galactic, extragalactic, and combined sets are 0.92 ± 0.13, 1.07 ± 0.06, and 0.98 ± 0.02 respectively. These slopes are all within 1σ of unity. The agreement between the extrapolated galactic and extragalactic best-fit lines is better than for HCO^+ (3-2). The extragalactic correlation from Gao & Solomon (2004a,b) spans 1.5 more orders of magnitude in L_{bol} than the observed HCO^+ (3-2) in galaxies and likely provides a more robust sample from which to determine the best-fit. Our re-analysis of the Gao & Solomon and Wu et al. data confirms their results.

[YLS - I'm confused by the results here - esp. what is wrong with DR21S and why Jingwen would have not included it without telling anyone. Also, how strong is the variation in slope and the cutoff moves to lower luminosities? I have not edited these last two paragraphs.] The amount of dense gas in the galactic clumps needs to be high enough to sample the IMF, forcing a lower limit of $L_{IR}=10^{4.5}$ $L_\odot$ (Wu et al. 2010). The correlations were found with this cutoff in order for direct comparison with previous results. The extragalactic set was unaffected by both cutoffs. The combined data set produced a slope of 0.94 ± 0.02, which is nearly in agreement with the unity slope determined using least squares linear fits. However, galactic data had a much lower slope of 0.55 ± 0.15. Part of the reason for the discrepancy may be that it appears an outlier, DR21S, was excluded from the fit in Wu (2010). Excluding DR21S raises the slope to 0.87 ± 0.15.

The fits were also derived with no cutoff. These fits included 6 points not included when the cutoff of $L_{bol}=10^3$ was used. All of these points lie below the fit to the rest of the data. The motivation behind excluding these The IMF describes the proportion of stars that have a mass in a certain interval and, generally, lower mass stars are more common. A cloud forming stars will have a population of stars with masses drawn from the IMF. A

cloud with a relatively small mass will not form as many stars which makes the probability of seeing a massive star lower. When we say "sample the IMF", we mean the probability of seeing stars at across the full range of the IMF is high. Larger clouds with more stars will be more luminous, so the cutoff can be expressed as a minimum luminosity. Krumholz and Thompson (2007) claim that the cloud mass should exceed ∼1000 $M_\odot$ to accomplish a decent sampling. The points in the top right plot of Figure 2 that lie below the cutoff also tend to lie below the correlation, meaning they are underluminous. This indicates a deficiency in forming massive stars and justifies instituting the cutoff.

5.3. Comparison to theory

The physical basis for the observed L′-L_{bol} correlations have been studied using numerical simulations. Krumholz and Thompson (2007) modeled isothermal and homogeneous giant molecular clouds (GMCs) using a radiative transfer code and considering star formation regulated by turbulence. Narayanan et al. (2010) used 3D non-LTE radiative transfer with hydrodynamic simulations of isolated galaxies and galaxy mergers. Despite considering two different classes of object, the same explanation was reached by both. The origin of the SFR-L′ relation comes from the Schmidt relationship and the density dependence of L′. The Schmidt relation says that the star formation rate is proportional to density to some power, or

$$SFR \propto \rho^N \tag{10}$$

where N is the Schmidt index. The value of N is 1.5 with one factor of ρ coming from the mass available for stars and a factor of $\rho^{0.5}$ coming from the dependence of the dynamical time for collapse on the density (Krumholz and Thompson 2007). This assumes star formation occurs at a constant rate per dynamical time. To predict the relation between SFR and line luminosity,

$$SFR \propto L'^{\alpha}, \tag{11}$$

the dependence of the line luminosity on density must be known. This is expressed as

$$L' \propto \rho^{\beta} \tag{12}$$

so that the index of the SFR-L′ correlation is $\alpha=\frac{N}{\beta}$.

Both simulations determined that density dependence of L′ fell into two regimes, one in which the critical density is much larger than the mean density of the gas and one in which it is much smaller. When $n_{crit} >> \bar{n}$, only the high density tail of the density distribution is above the critical density so emission predominantly arises from the densest regions. The emission does not trace the conditions in the gas, but instead will trace the same density

in every subcritical object. As density increases (with n_{crit} remaining much larger than $\bar{n}$), the line emission rises superlinearly so that $\beta > 1$ and $\alpha < N$. The SFR-L′ relation will have an index below the Schmidt index. Both HCO^+ (3-2) and HCN (1-0) fall in this regime. In the other case where $n_{crit} << \bar{n}$, nearly all of the gas is thermalized and emitting. The line luminosity faithfully traces the mass and rises linearly with density. The index of the SFR-L′ relation will approximately equal the Schmidt index. CO (1-0) produces an index near the Schmidt index, which is consistent with this formulation as CO traces lower densities than HCO^+ and HCN.

Some combinations of gas conditions and molecular transitions will be somewhere intermediate between the two cases. As density increases, the relation passes from the subcritical to the supercritical case, meaning the SFR-L′ relation should transition from linear to superlinear. Evidence of this upturn have been found in observations, though it is only tentative due to a caveat to be discussed in the next subsection.

A power law index of 1.0 was predicted for HCN (1-0), in agreement with observations. The critical density of HCO^+ (3-2) is about a factor of 3 higher than that of HCN (1-0), a small difference given that the n_{crit} of different tracers span several orders of magnitude. Based on the theoretical predictions, the index for HCO^+ (3-2) should also be near 1.0. The results presented in this paper are consistent with the theoretical predictions of Krumholz & Thompson and Narayanan et al.

5.4. Caveats

The L_{bol}-L′ relation is intended to represent a relation between the SFR and gas mass. However, the conversions are complicated by a wide range of assumptions which must be explored.

Bolometric (or infrared) luminosity is the most popular measure of the star formation rate (SFR) as it is easy to determine. On scales from 1 kpc to galactic scales, the IMF of stars is well sampled and conversion between L_{bol} and SFR is linear (see Kennicutt 1998). However, this conversion for galaxies is potentially confounded by the presence of active galactic nuclei (AGN). An AGN can contribute its own IR emission (Krumholz and Thompson 2007, Narayanan et al. 2008, Graciá-Carpio et al. 2008). The extra observed IR flux can lead to an overestimate of the SFR. The AGN contribution should be larger in more luminous galaxies which harbor more powerful AGN, leading to even greater overestimates. This effect would cause the most luminous galaxies to drift above the trend of the other sources. As mentioned before, both the GMC and galaxy models predict an upturn in the

relation, but this is due to the average density switching from below to above the critical density. In fact, neither model even considered AGN which can mimic the predicted upturn. Detailed modeling of the SEDs of galaxies that harbor AGN are needed to deconvolve the contribution to the bolometric luminosity from AGN and star formation.

While Galactic clumps will not be affected by AGN, their L_{bol} also is not a perfect measure of the SFR. The most massive stars in a system younger than ∼3 Myr will not have had time to evolve and die in a supernova; therefore, not enough time has elapsed to achieve equilibrium between stellar birth and death. A simulation run by Krumholz and Tan (2007) found that the luminosity per unit star formation is insensitive to the age for populations older than a few Myr (which is a timescale that is easily averaged over 1 kpc within a galaxy but would not necessarily apply on the scale of an individual Galactic clump). The luminosity of younger populations traced mass, but not the star formation rate. Dividing the mass by an independent measure of the age to estimate the star formation rate does not solve the problem for systems younger than ∼1 Myr because not all of the stars in such a system have finished collapsing. These pre-main sequence stars are powered by accretion and will release more energy than a main sequence star of the same mass. Since the contribution of these collapsing objects is unknown, it is impossible to determine how much mass is in the system (Krumholz and Tan 2007). By resolving the infrared population in Galactic clumps (e.g., with JWST or LBTI) and directly comparing the mass distribution within the clumps (e.g. with ALMA), we may be able to better constrain the actual SFR in Galactic clumps.

Chemical variation potentially make the utility of HCN and HCO^+ questionable as a uniform dense gas tracers in different environments. The strong X-ray emission from an AGN can increase ionization and therefore the abundance of HCN in relation to other molecules (Lintott et al. 2006). This is the explanation given for the trend observed in the HCN(1-0)/HCO^+(1-0) luminosity ratio which increases with increasing far-infrared luminosity for $L_{FIR} > 10^{11}$ $L_\odot$ by Graciá-Carpio et al. (2008). However, another interpretation is that more luminous galaxies have a higher dense gas fraction and the effects on HCN chemistry are negligible. Using 5 transitions from 3 molecules (HCN, HCO^+, CO) to form 10 line luminosity ratios (with the higher critical density tracer in the numerator), Juneau et al. (2009) showed that the ratios consistently increased with L_{IR} except for the HCO^+(3-2)/HCN(1-0) ratio which combines the two tracers considered here. This ratio which has tracers of nearly the same critical density was approximately constant. Using the same simulation as Narayanan (2008), the line ratio behavior was replicated without including chemical abundance changes. They concluded the dense gas fraction increased with luminosity and that inclusion of chemical effects in the dense gas were not necessary.

Molecular gas tracers are supposed to indicate the presence of the gas with which it

collides, emitting more energy when they undergo more collisions. Ideally, all emission would be a result of interactions with the gas, but the emission can be affected by the background radiation. The excitation of HCN lines may be enhanced by IR pumping of a 14 μm vibrational transition (Graciá-Carpio et al. 2006). Similarly, HCO^+ excitation can be affected by a 12 μm vibrational transition. Any emission associated with radiative pumping will to lead overestimates of the gas mass inferred from the line luminosity.

The complications discussed above present real obstacles to interpreting the L_{bol}-L' relation. None of them were included in the GMC or galaxy radiative transfer modeling because of the high degree of sophistication that each would require. It is argued in both Krumholz and Thompson (2007) and Narayanan et al. (2008) that their ability to replicate the relations for different tracers without accounting for these details shows that their effects may be negligible. Despite these caveats, the results form this study show similar trends for the L_{bol}-L' relation of HCO^+ (3-2) as was observed by Wu et al. (2005, 2010) for HCN (1-0).

6. Summary

We conclude that line luminosity in HCO^+ (3-2) is tracing mass as evidenced by the fits of L' with isothermal mass and virial mass. M_{vir} rises roughly linearly with L' while M_{iso} also increases with L', but with a sub-linear slope.

The slope of the $\log(L_{bol})$-$\log(L')$ relation is statistically consistent with unity for HCO^+ (3-2). A similar result was seen by Gao and Solomon (2004) and Wu et al. (2010) which both used HCN (1-0), a tracer with similar conditions for excitation as HCO^+ (3-2). An attempt was made to recreate their relations and while the galaxies gave a nearly unity slope in log-log space, the slope for the Galactic clumps was seen to depend strongly on the minimum luminosity cutoff imposed. The slope decreased as more low luminosity sources were excluded with a super-linear relation for no cutoff and a sub-linear relation for a cutoff of L_{IR}=$10^{4.5}$ $L_\odot$. [YLS - let's confirm and characterize this latter result.]

The results of our work are generally consistent with theoretical predictions from radiative transfer models. Two different models, one considering GMCs (Krumholz and Thompson 2007) and one considering isolated galaxies and galaxy mergers (Narayanan et al. 2008), predicted that the slope of the $\log(L_{bol})$-$\log(L')$ relation should depend on the critical density of the tracer and the mean density of the gas. If the critical density is above the mean gas density, then only high density peaks are thermalized and emit. In this case, the line luminosity rises super-linearly with density and the (L_{bol})-$\log(L')$ relation is linear. If the critical density of the tracer is below the mean gas density, then nearly all the gas is traced

and the line luminosity faithfully traces the gas, rising linearly with density. This leads to a super-linear L_{bol}-L′ relation. Both models predict a roughly linear relation for HCN (1-0) and since HCO^+ (3-2) is excited in similar conditions, it should behave similarly.

The conversions of L_{bol} to SFR has many caveats. It can be confounded by the presence of AGN boosting the luminosity by heating dust grains or radiatively pumping the gas tracers to cause excess line emission. Uncertainty in the age and ability to sample the IMF plague Galactic clumps. Ultimately, high resolution mid-infrared and submillimeter observations are needed to resolve embedded infrared populations and dense gas cores in Galactic clumps to reliably determine the SFR. All of these caveats must be considered and characterized before the underlying star formation relation can be fully understood.

Our study suffered from a small sample of galaxies mapped in HCO^+ (3-2). Only 14 were available from Juneau et al. (2009) who obtained them from the original work done by Graciá-Carpio et al. (2008). A more complete survey must be conducted to fill in the sparsely populated high luminosity corner of the L_{bol}-L′ plot. A followup extragalatic survey should include galaxies that span a wider range in L_{bol}.

Acknowledgements The authors would like to acknowledge John Downey, Sean Keel, Robert Moulton for operating the HHT during our observations. We thank Brandon Kelly for explaining the details of the Bayesian linear regression program. We also thank Timothy Ellsworth-Bowers for sharing his work in distance determination prior to publication. Yancy Shirley is partially supported by NSF grant AST-1008577.

REFERENCES

Andre, P., Ward-Thompson, D., & Barsony, M. 2000, Protostars and Planets IV, 59

Battersby, C., Bally, J., Jackson, J. M., Ginsburg, A., Shirley, Y. L., Schlingman, W., & Glenn, J. 2010, ApJ, 721, 222

Bertoldi, F., & McKee, C. F. 1992, ApJ, 395, 140

Bigiel, F., et al. 2011, ApJ, 730, L13

Bussmann, R. S., et al. 2008, ApJ, 681, L73

Cheung, L. H., Frogel, J. A., Hauser, M. G., & Gezari, D. Y. 1980, ApJ, 240, 74

Chini, R., Henning, T., & Pfau, W. 1991, A&A, 247, 157

Chini, R., Kreysa, E., Mezger, P. G., & Gemuend, H.-P. 1986a, A&A, 154, L8

Dent, W. R. F., Matthews, H. E., & Ward-Thompson, D. 1998, MNRAS, 301, 1049

Di Francesco, J., Johnstone, D., Kirk, H., MacKenzie, T., & Ledwosinska, E. 2008, ApJS, 175, 277

Dyck, H. M., & Simon, T. 1977, ApJ, 211, 421

Ellis, H. B., Jr., Lester, D. F., Harvey, P. M., Joy, M., Telesco, C. M., Decher, R., & Werner, M. W. 1990, ApJ, 365, 287

Enoch, M. L., et al. 2006, ApJ, 638, 293

Evans, N. J., II, et al. 1981, ApJ, 244, 115

Evans, N. J., II 1999, ARA&A, 37, 311

Evans, N. J., II, Beckwith, S., Brown, R. L., & Gilmore, W. 1979, ApJ, 227, 450

Fazio, G. G., Lada, C. J., Kleinmann, D. E., Wright, E. L., Ho, P. T. P., & Low, F. J. 1978, ApJ, 221, L77

Gao, Y., & Solomon, P. M. 2004, ApJ, 606, 271

Gordon, M. A. 1990, ApJ, 352, 636

Graciá-Carpio, J., García-Burillo, S., Planesas, P., & Colina, L. 2006, ApJ, 640, L135

Graciá-Carpio, J., García-Burillo, S., Planesas, P., Fuente, A., & Usero, A. 2008, A&A, 479, 703

Guertler, J., Henning, T., Kruegel, E., & Chini, R. 1991, A&A, 252, 801

Hastings, W. K. 1970, Biometrika, 57, 97

Hatchell, J., Fuller, G. A., Millar, T. J., Thompson, M. A., & Macdonald, G. H. 2000, A&A, 357, 637

IRAS PSC 1988, ed. C. Beichman et al. (NASA RP-1190; Washington: GPO)

Jaffe, D. T., Hildebrand, R. H., Keene, J., Harper, D. A., Loewenstein, R. F., & Moran, J. M. 1984, ApJ, 281, 225

Jenness, T. 1996, Ph.D. Thesis

Jenness, T., Scott, P. F., & Padman, R. 1995, MNRAS, 276, 1024

Juneau, S., Narayanan, D. T., Moustakas, J., Shirley, Y. L., Bussmann, R. S., Kennicutt, R. C., & Vanden Bout, P. A. 2009, ApJ, 707, 1217

Kelly, B. C. 2007, ApJ, 665, 1489

Kennicutt, R. C., Jr. 1998, ApJ, 498, 541

Krumholz, M. R., & Tan, J. C. 2007, ApJ, 654, 304

Krumholz, M. R., & Thompson, T. A. 2007, ApJ, 669, 289

Lintott, C., & Viti, S. 2006, ApJ, 646, L37

Mangum, J. G., Emerson, D. T., & Greisen, E. W. 2007, A&A, 474, 679

Mangum, J. G., Darling, J., Menten, K. M., & Henkel, C. 2008, ApJ, 673, 832

McCutcheon, W. H., Sato, T., Purton, C. R., Matthews, H. E., & Dewdney, P. E. 1995, AJ, 110, 1762

McKee, C. F., & Ostriker, E. C. 2007, ARA&A, 45, 565

Metropolis, N., Rosenbluth, A. W., Rosenbluth, M. N., Teller, A. H., & Teller, E. 1953, J. Chem. Phys., 21, 1087

Mookerjea, B., Ghosh, S. K., Karnik, A. D., Rengarajan, T. N., Tandon, S. N., & Verma, R. P. 1999, ApJ, 522, 285

Moriarty-Schieven, G. H., Snell, R. L., & Hughes, V. A. 1991, ApJ, 374, 169

Mottram, J. C., Hoare, M. G., Lumsden, S. L., Oudmaijer, R. D., Urquhart, J. S., Meade, M. R., Moore, T. J. T., & Stead, J. J. 2010, A&A, 510, A89

Mueller, K. E., Shirley, Y. L., Evans, N. J., II, & Jacobson, H. R. 2002, ApJS, 143, 469

Narayanan, D., Cox, T. J., Shirley, Y., Davé, R., Hernquist, L., & Walker, C. K. 2008, ApJ, 684, 996

Ossenkopf, V., & Henning, T. 1994, A&A, 291, 943

Phillips, T. G., Huggins, P. J., Wannier, P. G., & Scoville, N. Z. 1979, ApJ, 231, 720

Schlingman, W. M., et al. 2011, Bulletin of the American Astronomical Society, 43, #411.03

Shirley, Y. L., Evans, N. J., II, Young, K. E., Knez, C., & Jaffe, D. T. 2003, ApJS, 149, 375

Shirley, Y. L., Wu, J., Shane Bussmann, R., & Wootten, A. 2008, Massive Star Formation: Observations Confront Theory, 387, 401

Shu, F. H., Adams, F. C., & Lizano, S. 1987, ARA&A, 25, 23

Soifer, B. T., & Pipher, J. L. 1975, ApJ, 199, 663

Stier, M. T., et al. 1984, ApJ, 283, 573

Tothill, N. F. H. 1999, Ph.D. Thesis

Werner, M. W., Becklin, E. E., Gatley, I., Matthews, K., Neugebauer, G., & Wynn-Williams, C. G. 1979, MNRAS, 188, 463

Wu, J., Evans, N. J., Shirley, Y. L., & Knez, C. 2010, ApJS, 188, 313

Zhou, S., Butner, H. M., Evans, N. J., II, Guesten, R., Kutner, M. L., & Mundy, L. G. 1994, ApJ, 428, 219

Table 1. Source Properties

Source	α (J2000) [h m s]	δ (J2000) [° ′ ″]	$\log(L_{bol}$ or $L_{IR})$ [$L_\odot$]	Distance [kpc]	Distance [1] Comment
019.884-053	18 29 14.3	-11 50 22.8	5.15 ± 0.01	12.47 ± 0.27	Complex
028.861+006	18 43 46.3	-3 35 31.6	5.01 ± 0.00	5.46 ± 0.26	Complex
027.187-008	18 41 13.2	-5 8 58.1	5.38 ± 0.01	12.93 ± 0.33	Complex
029.436-017	18 45 40.6	-3 11 21.4	3.44 ± 0.03	4.87 ± 0.24	IRDC
019.923-025	18 28 18.9	-11 40 31.2	3.48 ± 0.02	4.25 ± 0.21	IRDC-Complex
024.730+015	18 35 50.6	-7 13 26.4	4.51 ± 0.02	5.77 ± 0.20	Complex
034.712-059	18 56 48.2	1 18 45.6	3.83 ± 0.01	2.80 ± 0.28	Complex
027.925+020	18 41 34.5	-4 21 7.9	3.83 ± 0.01	2.86 ± 0.29	Complex
037.555+019	18 59 10	4 12 18.4	4.64 ± 0.01	5.59 ± 0.37	Complex
059.497-023	19 43 42.3	23 20 19	3.48 ± 0.01	3.27 ± 0.68	IRDC
033.384+000	18 52 14.5	0 24 54.5	4.20 ± 0.07	6.35 ± 0.34	IRDC
025.803-015	18 38 56.5	-6 24 53.4	4.71 ± 0.01	5.20 ± 0.22	Complex
025.411+010	18 37 17	-6 38 28.1	3.97 ± 0.02	5.26 ± 0.20	Complex
059.355-020	19 43 17.9	23 13 58.9	4.11 ± 0.01	4.04 ± 0.68	Complex
025.393+004	18 37 30.3	-6 41 14.8	3.37 ± 0.01	1.11 ± 0.28	
023.385+018	18 33 14.6	-8 23 55.6	4.33 ± 0.01	4.51 ± 0.21	Complex
121.30+0.66	0 36 48	63 29 1	3.09 ± 0.02	0.85 ± 0.42	
123.07-6.31	0 52 25	56 33 53	3.74 ± 0.04	2.2 ± 0.4	
W3(OH)	2 27 5	61 52 26	4.99 ± 0.01	2.4 ± 0.4	
S231	5 39 13	35 45 54	4.00 ± 0.02	2.0 ± 0.4	
S252A	6 8 35	20 39 3	4.32 ± 0.00	1.5 ± 0.4	
RCW142	17 50 15	-28 54 32	4.68 ± 0.04	2.0 ± 0.4	
W28A2	18 0 30	-24 3 58	5.44 ± 0.05	2.6 ± 0.4	
M8E	18 4 53	-24 26 42	4.21 ± 0.02	1.8 ± 0.4	
8.67-0.36	18 6 19	-21 37 38	5.08 ± 0.03	4.5 ± 0.5	
10.60-0.40	18 10 29	-19 55 49	5.99 ± 0.04	6.5 ± 0.5	
12.89+0.49	18 11 51	-17 31 31	4.55 ± 0.01	3.5 ± 0.4	
W33A	18 14 39	-17 52 11	5.12 ± 0.01	4.5 ± 0.4	
24.49-0.04	18 36 5	-7 31 23	4.69 ± 0.01	3.5 ± 0.2	
W43S	18 46 4	-2 39 26	6.10 ± 0.02	8.5 ± 0.3	
31.41+0.31	18 47 34	-1 12 46	5.27 ± 0.03	7.9 ± 0.3	
W44	18 53 18	1 14 57	5.58 ± 0.03	3.7 ± 0.3	
40.50+2.54	18 56 10	7 53 14	4.29 ± 0.05	2.1 ± 0.4	
35.20-0.74	18 58 13	1 40 36	4.76 ± 0.05	3.3 ± 0.4	
59.78+0.06	19 43 12	23 43 54	4.02 ± 0.03	2.2 ± 0.6	
ON1	20 10 9	31 31 37	5.11 ± 0.02	6.0 ± 0.4	
ON2S	20 21 41	37 25 29	5.59 ± 0.02	5.5 ± 0.4	

Table 1—Continued

Source	α (J2000) [h m s]	δ (J2000) [° ′ ″]	log(L_{bol} or L_{IR}) [$L_\odot$]	Distance [kpc]	Distance [1] Comment
W75N	20 38 37	42 37 37	5.29 ± 0.03	3.0 ± 0.4	
W75OH	20 39 1	42 22 50	4.40 ± 0.02	3.0 ± 0.4	
S140	22 19 18	63 18 47	4.34 ± 0.02	0.9 ± 0.4	
CepA	22 56 18	62 1 46	4.52 ± 0.02	0.73 ± 0.42	
NGC7538-IRS9	23 14 2	61 27 20	4.59 ± 0.05	2.8 ± 0.7	
S157	23 16 4	60 1 41	4.31 ± 0.03	2.5 ± 0.7	
Mean			5.09	4.11	
Standard Deviation			0.87	2.67	
Median			4.52	3.5	

[1]IRDC: The source is associated with an infrared dark cloud. The near kinematic distance was assigned. Complex: The source is a part of a complex with a known distance. If one of the kinematic distances was similar to the complex distance, that kinematic distance was assigned (Mottram et al. 2010).

Table 2. HCO^+ Properties

Source	I [$K\ km\ s^{-1}$]	v_{LSR} [$km\ s^{-1}$]	θ_{s*b} [″]	R [pc]	log(L′) [$K\ km\ s^{-1}\ pc^{-2}$]
019.884-053	46.12 ± 2.47	43.99	41.8 ± 3.3	0.96 ± 0.13	2.52 ± 0.07
028.861+006	16.91 ± 0.94	103.90	38.6 ± 3.1	0.36 ± 0.06	1.30 ± 0.09
027.187-008	15.07 ± 0.87	25.65	29.3 ± 3.1	0.34 ± 0.27	1.76 ± 0.10
029.436-017	3.17 ± 0.36	86.19	36.7 ± 11.0	0.29 ± 0.19	0.43 ± 0.27
019.923-025	7.54 ± 0.48	64.30	46.3 ± 7.8	0.39 ± 0.10	0.89 ± 0.16
024.730+015	5.65 ± 0.44	109.61	32.6 ± 6.1	0.25 ± 0.16	0.73 ± 0.17
034.712-059	9.03 ± 0.59	44.17	46.4 ± 5.5	0.26 ± 0.05	0.61 ± 0.14
027.925+020	12.45 ± 0.76	42.65	34.8 ± 2.7	0.15 ± 0.03	0.52 ± 0.11
037.555+019	13.67 ± 0.83	86.21	44.0 ± 4.5	0.47 ± 0.08	1.34 ± 0.11
059.497-023	17.03 ± 0.97	27.13	44.4 ± 5.1	0.28 ± 0.08	0.98 ± 0.21
033.384+000	11.14 ± 0.67	103.88	40.5 ± 4.2	0.46 ± 0.09	1.29 ± 0.10
025.803-015	16.41 ± 0.94	92.06	39.4 ± 3.4	0.36 ± 0.06	1.26 ± 0.09
025.411+010	12.10 ± 0.74	95.91	37.7 ± 3.2	0.33 ± 0.06	1.10 ± 0.09
059.355-020	10.52 ± 0.69	29.53	49.0 ± 5.0	0.40 ± 0.09	1.04 ± 0.17
025.393+004	11.27 ± 0.66	-13.02	34.9 ± 2.8	0.06 ± 0.02	-0.34 ± 0.23
023.385+018	9.96 ± 0.71	75.75	37.9 ± 4.0	0.29 ± 0.06	0.89 ± 0.11
Mean	13.63			0.35	1.53
Standard Deviation	9.51			0.19	1.05
Median	11.69			0.34	1.01

Table 3. HCO^+ Properties

Source	Δv $[km\ s^{-1}]$	$\log(M_{iso})$ $[M_\odot]$	$\log(M_{vir})$ $[M_\odot]$
019.884-053	5.8 ± 0.1	3.99 ± 0.04	3.69 ± 0.06
028.861+006	5.7 ± 0.1	3.05 ± 0.05	3.25 ± 0.07
027.187-008	7.4 ± 0.3	3.63 ± 0.05	3.44 ± 0.35
029.436-017	3.4 ± 0.2	2.28 ± 0.08	2.70 ± 0.30
019.923-025	4.8 ± 0.2	2.71 ± 0.05	3.13 ± 0.12
024.730+015	3.7 ± 0.2	2.61 ± 0.07	2.72 ± 0.27
034.712-059	9.0 ± 0.7	2.20 ± 0.09	3.50 ± 0.11
027.925+020	4.9 ± 0.2	2.06 ± 0.10	2.73 ± 0.10
037.555+019	8.9 ± 0.3	2.98 ± 0.07	3.75 ± 0.08
059.497-023	3.4 ± 0.1	2.10 ± 0.20	2.69 ± 0.12
033.384+000	4.8 ± 0.2	2.99 ± 0.06	3.20 ± 0.09
025.803-015	3.7 ± 0.2	2.67 ± 0.06	2.86 ± 0.09
025.411+010	6.9 ± 0.2	2.52 ± 0.07	3.38 ± 0.08
059.355-020	2.8 ± 0.1	1.82 ± 0.26	2.67 ± 0.10
025.393+004	7.3 ± 0.2	1.37 ± 0.22	2.68 ± 0.14
023.385+018	3.8 ± 0.1	2.58 ± 0.06	2.80 ± 0.10
Mean		3.09	3.24
Standard Deviation		0.87	0.41
Median		2.60	3.01

Table 4. Photometry

Source	λ [μm]	Flux [Jy]	Beam [$''$]	Ref [1]
019.884-053	8	0.613 ± 0.03	18	1
	14	0.73 ± 0.06	18	1
	21	3.43 ± 0.22	18	1
	25	11.07±	300x45	2
	60	394.45 ± 3.75	165x87	3
	65	285.489 ± 41.202	600x60	4
	70	407.22 ± 2.99	62.4	3
	90	211.589 ± 38.44	600x90	4
	100	1155.65 ± 6.07	195x150	3
	140	598.963 ± 37.254	700x100	4
	160	794.996 ± 115.704	700x150	4
	850	8.24±	13.5	5
	1100	4.91 ± 0.368	33	6
028.861+006	8	3.284 ± 0.13	18	1
	12	7.12 ± 0.36	18	1
	14	15.34 ± 0.94	18	1
	21	34.01 ± 2.04	18	1
	25	105.2±	300x45	2
	60	1945.55 ± 7.08	165x87	3
	65	1493.04 ± 176.252	600x60	4
	70	1567.44 ± 3.73	62.4	3
	90	1207.87 ± 88.651	600x90	4
	100	3263.03 ± 19.92	195x150	3
	140	839.887 ± 2.288	700x100	4
	1100	4.385 ± 0.292	33	6
027.187-008	8	1.345 ± 0.06	18	1
	12	3.06 ± 0.16	18	1
	14	5.22 ± 0.32	18	1
	21	16.77 ± 1.01	18	1
	25	39.2±	300x45	2
	60	797.61 ± 6.92	165x87	3
	65	527.153 ± 98.697	600x60	4
	70	640.54 ± 3.38	62.4	3
	90	360.934 ± 120.562	600x90	4
	100	1634.41 ± 14.9	195x150	3
	140	447.085 ± 32.62	700x100	4
	160	562.541 ± 84.363	700x150	4

Table 4—Continued

Source	λ [μm]	Flux [Jy]	Beam [$''$]	Ref [1]
	1100	2.203 ± 0.224	33	6
029.436-017	8	1.332 ± 0.05	18	1
	12	1.6 ± 0.1	18	1
	14	2.33 ± 0.15	18	1
	21	3.18 ± 0.2	18	1
	65	22.21 ± 3.152	600x60	4
	70	18.39 ± 4.16	62.4	3
	90	24.279 ± 0.653	600x90	4
	160	130.82 ± 22.811	700x150	4
	1100	0.67 ± 0.135	33	6
019.923-025	8	0.952 ± 0.04	18	1
	12	2.33 ± 0.13	18	1
	14	4.15 ± 0.25	18	1
	21	5.5 ± 0.34	18	1
	25	$6.741\pm$	300x45	2
	60	13.94 ± 2.27	165x87	3
	70	35.4 ± 3.19	62.4	3
	90	32.141 ± 1.064	600x90	4
	100	315.19 ± 23.91	195x150	3
	140	96.555 ± 9.745	700x100	4
	160	140.926 ± 22.972	700x150	4
	1100	3.022 ± 0.224	33	6
024.730+015	8	1.169 ± 0.05	18	1
	12	1.52 ± 0.08	18	1
	14	1.74 ± 0.11	18	1
	21	5.44 ± 0.33	18	1
	25	$15.2\pm$	300x45	2
	60	$325.5\pm$	90x300	2
	65	177.776 ± 7.83	600x60	4
	70	188.39 ± 4.32	62.4	3
	100	$1279\pm$	180x300	2
	140	649.826 ± 62.512	700x100	4
	160	749.966 ± 72.178	700x150	4
	1100	1.392 ± 0.189	33	6
034.712-059	8	8.131 ± 0.33	18	1
	12	10.26 ± 0.51	18	1
	14	13 ± 0.79	18	1

Table 4—Continued

Source	λ [μm]	Flux [Jy]	Beam [$''$]	Ref [1]
	21	26.89 ± 1.61	18	1
	25	43.7±	300x45	2
	60	290.98 ± 2.48	165x87	3
	65	295.412 ± 63.667	600x60	4
	70	250.61 ± 3.2	62.4	3
	90	178.623 ± 65.615	600x90	4
	100	1086.15 ± 9.72	195x150	3
	140	265.165 ± 33.812	700x100	4
	1100	2.458±	33	6
027.925+020	8	0.938 ± 0.04	18	1
	12	1.14 ± 0.08	18	1
	14	1.68 ± 0.11	18	1
	21	6.49 ± 0.4	18	1
	60	402.72 ± 2.33	165x87	3
	65	264.639 ± 22.527	600x60	4
	70	218.93 ± 3.17	62.4	3
	90	275.781 ± 2.759	600x90	4
	100	1137.67 ± 10.42	195x150	3
	140	304.938 ± 53.185	700x100	4
	160	404.624 ± 31.684	700x150	4
	1100	1.855 ± 0.167	33	6
037.555+019	8	8.573 ± 0.35	18	1
	12	14.83 ± 0.74	18	1
	14	24.74 ± 1.51	18	1
	21	37.87 ± 2.27	18	1
	25	85.25±	300x45	2
	60	538.36 ± 5.57	165x87	3
	65	380.241 ± 128.671	600x60	4
	70	510.17 ± 3.26	62.4	3
	90	288.244 ± 104.528	600x90	4
	100	937.88 ± 10.59	195x150	3
	140	429.701 ± 86.895	700x100	4
	160	537.719 ± 143.92	700x150	4
	850	5.45±	13.5	5
	1100	3.106 ± 0.254	33	6
059.497-023	8	0.075 ± 0.01	18	1
	12	1.07 ± 0.52	18	1

Table 4—Continued

Source	λ [μm]	Flux [Jy]	Beam [$''$]	Ref [1]
	14	1.65 ± 0.11	18	1
	21	4.66 ± 0.29	18	1
	25	$10.71\pm$	300x45	2
	60	122.4 ± 1.07	165x87	3
	65	64.528 ± 9.104	600x60	4
	70	33.92 ± 3.98	62.4	3
	90	37.466 ± 7.779	600x90	4
	100	462.16 ± 4.8	195x150	3
	140	96.32 ± 39.963	700x100	4
	160	192.869 ± 20.754	700x150	4
	1100	1.374 ± 0.231	33	6
033.384+000	8	0.067 ± 0.007	18	1
	12	0.21 ± 0.02	18	1
	14	1.22 ± 0.07	18	1
	21	5.27 ± 0.32	18	1
	65	122.77 ± 35.072	600x60	4
	70	124.36 ± 4.99	62.4	3
	90	145.519 ± 15.973	600x90	4
	140	279.367 ± 76.98	700x100	4
	160	399.491 ± 143.585	700x150	4
	1100	4.128 ± 0.276	33	6
025.803-015	8	2.256 ± 0.09	18	1
	12	8.55 ± 0.43	18	1
	14	18.27 ± 1.11	18	1
	21	68.66 ± 4.12	18	1
	60	790.5 ± 6.81	165x87	3
	65	349.181 ± 35.482	600x60	4
	70	417.27 ± 4.03	62.4	3
	90	345.45 ± 60.751	600x90	4
	100	1846.48 ± 16.71	195x150	3
	140	351.462 ± 120.177	700x100	4
	160	282.206 ± 135.445	700x150	4
	850	$4.95\pm$	13.5	5
	1100	1.898 ± 0.191	33	6
025.411+010	8	2.327 ± 0.1	18	1
	12	3.46 ± 0.17	18	1
	14	4.7 ± 0.29	18	1

Table 4—Continued

Source	λ [μm]	Flux [Jy]	Beam [$''$]	Ref [1]
	21	8.43 ± 0.51	18	1
	25	17.5±	300x45	2
	60	109.9±	90x300	2
	65	152.964 ± 10.846	600x60	4
	70	142.1 ± 3.36	62.4	3
	90	75.81 ± 11.842	600x90	4
	140	157.186 ± 43.685	700x100	4
	160	279.51 ± 30.236	700x150	4
	1100	1.012 ± 0.162	33	6
059.355-020	8	1.818 ± 0.07	18	1
	12	5.24 ± 0.27	18	1
	14	8.72 ± 0.53	18	1
	21	25.6 ± 1.54	18	1
	25	41.16±	300x45	2
	60	333.15 ± 1.9	165x87	3
	70	87.5 ± 3.36	62.4	3
	100	879.54 ± 7.21	195x150	3
	140	187.368 ± 40.365	700x100	4
	1100	0.379 ± 0.201	33	6
025.393+004	8	2.287 ± 0.09	18	1
	12	4.78 ± 0.24	18	1
	14	7.14 ± 0.44	18	1
	21	17 ± 1.02	18	1
	60	1116.91 ± 8.23	165x87	3
	65	430.667 ± 115.065	600x60	4
	70	804.15 ± 4.61	62.4	3
	90	307.233 ± 59.003	600x90	4
	100	2350.42 ± 26.44	195x150	3
	140	569.916 ± 45.479	700x100	4
	160	662.995 ± 90.056	700x150	4
	1100	2.307 ± 0.222	33	6
023.385+018	8	23.468 ± 0.96	18	1
	12	39 ± 1.95	18	1
	14	50.99 ± 3.11	18	1
	21	54.71 ± 3.28	18	1
	25	76.45±	300x45	2
	60	281.63 ± 2.84	165x87	3

Table 4—Continued

Source	λ [μm]	Flux [Jy]	Beam [$''$]	Ref [1]
	65	262.221 ± 38.114	600x60	4
	70	239.14 ± 3.44	62.4	3
	100	157.45 ± 16.07	195x150	3
	160	331.908 ± 25.575	700x150	4
	1100	2.262 ± 0.211	33	6
121.30+0.66	12	1.8 ± 0.2	300x45	2
	25	21 ± 1	300x45	2
	60	357 ± 21	90x300	2
	90	790.329 ± 88.025	600x90	4
	100	685 ± 55	180x300	2
	140	843.326 ± 70.254	700x100	4
	143	1615 ± 323	105	7
	185	2317 ± 463	102	7
	350	410 ± 82	120	8
	450	49 ± 2	18	9
	800	6.2 ± 0.02	16	9
	850	17 ± 3.4	18	10
	1100	5.6 ± 1.1	18	11
123.07-6.31	25	13 ± 1	300x45	2
	60	330 ± 46	90x300	2
	65	263.844 ± 73.242	600x60	4
	100	1166 ± 117	180x300	2
	140	796.873 ± 277.152	700x100	4
	160	784.666 ± 319.666	700x150	4
	350	290 ± 58	120	8
W3(OH)	12	40.58 ± 4.058	300x45	2
	20	270 ± 27	49	8
	25	670 ± 67	49	8
	30	1400 ± 140	49	8
	40	4000 ± 400	49	8
	60	7000 ± 700	49	8
	65	6918.19 ± 198.058	600x60	4
	70	8500 ± 850	49	8
	100	9000 ± 900	49	8
	140	6700 ± 670	49	8
	160	8645.55 ± 1006.47	700x150	4
	180	4900 ± 490	49	8

Table 4—Continued

Source	λ [μm]	Flux [Jy]	Beam [$''$]	Ref [1]
	200	4100 ± 410	49	8
	250	2400 ± 240	49	8
	300	1400 ± 140	49	8
	350	1130 ± 230	120	8
	500	250 ± 25	49	8
	600	135 ± 14	49	8
	800	51 ± 5.1	49	8
	1000	24 ± 2.4	49	8
S231	12	5.6 ± 0.2	300x45	2
	25	75 ± 3.7	300x45	2
	60	722 ± 72	90x300	2
	100	1310 ± 131	180x300	2
	160	1841.75 ± 94.635	700x150	4
	350	522 ± 100	120	8
S252A	12	16 ± 0.6	300x45	2
	25	77 ± 3	300x45	2
	60	10321 ± 34	90x300	2
	100	1715 ± 189	180x300	2
	140	844.937 ± 131.429	700x100	4
	350	320 ± 64	120	8
RCW142	12	$42 \pm >$	300x45	2
	25	$281 \pm >$	300x45	2
	60	5476 ± 986	90x300	2
	65	2623.98 ± 59.427	600x60	4
	90	1616.73 ± 134.917	600x90	4
	100	13129 ± 1313	180x300	2
	160	8480.46 ± 824.936	700x150	4
	350	670 ± 130	120	8
W28A2	12	199 ± 12	300x45	2
	25	2190 ± 131	300x45	2
	60	12790 ± 3198	90x300	2
	100	26780 ± 6695	180x300	2
	350	1580 ± 320	120	8
M8E	12	118.6 ± 11.86	300x45	2
	25	289 ± 17	300x45	2
	60	1611 ± 226	90x300	2
	65	658.413 ± 610.008	600x60	4

Table 4—Continued

Source	λ [μm]	Flux [Jy]	Beam [$''$]	Ref [1]
	69	$2600 \pm N$	54	12
	90	805.25 ± 355.311	600x90	4
	100	2783 ± 696	180x300	2
	140	1570.57 ± 90.777	700x100	4
	160	2481.1 ± 263.064	700x150	4
	350	380 ± 76	120	8
	450	42 ± 15.8	19	13
	850	9 ± 1.01	25	13
8.67-0.36	12	18.95 ± 1.895	300x45	2
	25	254 ± 8	300x45	2
	60	1895 ± 303	90x300	2
	65	1151.07 ± 94.817	600x60	4
	100	5125 ± 1128	180x300	2
	140	2623.88 ± 312.826	700x100	4
	350	650 ± 130	120	8
	450	390 ± 98	18	10
	850	49 ± 10	18	10
	1300	7.1 ± 0.71	90	14
10.60-0.40	12	$23\pm >$	300x45	2
	25	$148\pm >$	300x45	2
	60	9479 ± 948	90x300	2
	69	$14000 \pm N$	90	15
	100	21375 ± 3847	180x300	2
	350	1900 ± 380	120	8
	1300	$26 \pm N$	90	16
12.89+0.49	20	30 ± 3	49	17
	40	360 ± 36	49	17
	59	1100 ± 110	49	17
	65	1399.45 ± 191.257	600x60	4
	90	1306.75 ± 98.748	600x90	4
	101	2200 ± 220	49	17
	135	2370 ± 237	49	17
	140	1179.4 ± 321.365	700x100	4
	180	2370 ± 237	49	17
	350	340 ± 68	120	8
	400	210 ± 21	49	17
	450	200 ± 50	18	18

Table 4—Continued

Source	λ [μm]	Flux [Jy]	Beam [$''$]	Ref [1]
W33A	20	113 ± 11	49	19
	25	268 ± 21	300x45	2
	33	539 ± 36	6.8	20
	40	1000 ± 100	49	8
	42	1300 ± 130	60	21
	59	2350 ± 235	49	8
	73	3400 ± 340	60	21
	77	4100 ± 410	60	21
	101	4050 ± 405	49	8
	135	4000 ± 400	60	2
	180	2750 ± 275	49	8
	350	960 ± 190	120	8
	400	300 ± 30	49	7
	450	240 ± 60	18	22
	850	45 ± 9	18	22
	1000	41 ± 8	65	23
	1300	$11 \pm N$	90	14
24.49-0.04	12	15.5 ± 2.2	300x45	2
	25	81 ± 8.1	300x45	2
	60	1476 ± 88	90x300	2
	100	3514 ± 14	180x300	2
	350	190 ± 37	120	8
W43S	12	218 ± 20	300x45	2
	12.5	$235 \pm N$	22	24
	12.6	$121 \pm N$	2	24
	19	$610 \pm N$	12	24
	25	1697 ± 136	300x45	2
	60	7501 ± 525	90x300	2
	65	3568.9 ± 1118.72	600x60	4
	90	1721.62 ± 679.201	600x90	4
	100	11669 ± 3151	180x300	2
	140	3374.24 ± 335.96	700x100	4
	160	2945.65 ± 1033.27	700x150	4
	350	440 ± 88	120	8
	1300	$8 \pm N$	90	14
31.41+0.31	25	52 ± 5.2	300x45	2
	60	1093 ± 197	90x300	2

Table 4—Continued

Source	λ [μm]	Flux [Jy]	Beam [$''$]	Ref [1]
	65	1272.43 ± 176.354	600x60	4
	90	1271.51 ± 187.273	600x90	4
	100	2815 ± 394	180x300	2
	140	1867.15 ± 192.685	700x100	4
	350	740 ± 150	120	8
	450	84 ± 17	9	25
	850	27 ± 1.4	15	25
	1350	4.9 ± 1	22	25
	2000	2.9 ± 0.6	34	25
W44	12	140.2 ± 14.02	300x45	2
	25	1106 ± 110.6	300x45	2
	60	11500 ± 1150	90x300	2
	65	5870.26 ± 968.91	600x60	4
	100	32460 ± 3246	180x300	2
	140	6928.97 ± 2480.48	700x100	4
40.50+2.54	12	31.8 ± 4.5	300x45	2
	25	242 ± 24	300x45	2
	60	2351 ± 423	90x300	2
	65	475.714 ± 124.255	600x60	4
	90	459.523 ± 304.483	600x90	4
	100	4218 ± 840	180x300	2
	140	920.727 ± 84.863	700x100	4
	160	1524.35 ± 368.281	700x150	4
	350	240 ± 48	120	8
	450	215 ± 54	18	10
	850	33 ± 7	18	10
35.20-0.74	12	4.262 ± 0.4262	300x45	2
	60	1930 ± 193	90x300	2
	90	1929.47 ± 60.96	600x90	4
	100	1124 ± 112.4	180x300	2
	140	3046.32 ± 629.556	700x100	4
	160	4930 ± 687.842	700x150	4
59.78+0.06	12	14.43 ± 1.443	300x45	2
	25	108.8 ± 10.88	300x45	2
	60	982.5 ± 98.25	90x300	2
	100	1631 ± 163.1	180x300	2
ON1	12	1.1 ± 0.1	300x45	2

Table 4—Continued

Source	λ [μm]	Flux [Jy]	Beam [$''$]	Ref [1]
	25	58.8 ± 4.7	300x45	2
	60	1431 ± 115	90x300	2
	65	1216.1 ± 99.834	600x60	4
	90	928.235 ± 70.579	600x90	4
	100	3119 ± 312	180x300	2
	160	2704.73 ± 138.89	700x150	4
	350	650 ± 130	120	8
ON2S	12	74 ± 4.5	300x45	2
	25	481 ± 29	300x45	2
	60	5446 ± 545	90x300	2
	100	$6985 \pm >$	180x300	2
	350	510 ± 100	120	8
	1300	$9 \pm N$	90	16
W75N	12	44.91 ± 4.491	300x45	2
	25	757.8 ± 75.78	300x45	2
	60	12160 ± 1216	90x300	2
	100	15950 ± 1595	180x300	2
W75OH	65	1753.16 ± 266.681	600x60	4
	90	1398.82 ± 346.788	600x90	4
	140	6880.15 ± 315.175	700x100	4
	160	12253.6 ± 2280.54	700x150	4
S140	12	332 ± 40	30	26
	20	740 ± 185	3.5	26
	25	1694 ± 170	30	26
	35	5700 ± 1425	34	26
	53	8200 ± 2050	17	26
	62	7600 ± 130	49	26
	76	9200 ± 150	49	26
	80	9900 ± 2475	37	26
	101	7700 ± 150	49	26
	111	7500 ± 150	49	26
	162	4700 ± 120	49	26
	175	54001 ± 350	45	26
	350	1210 ± 240	120	8
	400	3508 ± 8	49	26
	1300	1.4 ± 0.25	30	22
CepA	12	170 ± 60	300x45	2

Table 4—Continued

Source	λ [μm]	Flux [Jy]	Beam [$''$]	Ref [1]
	25	860 ± 215	300x45	2
	50	10600 ± 2650	20	27
	60	17000 ± 3400	90x300	2
	65	6375.83 ± 450.355	600x60	4
	100	230004 ± 600	180x300	2
	125	33100 ± 9170	50	28
	140	7456.13 ± 401.774	700x100	4
	160	10029.3 ± 1295.15	700x150	4
	350	1500 ± 300	120	8
	400	2570 ± 741	50	28
	450	737 ± 140	20	29
	800	86 ± 10	20	29
	1300	26 ± 8	40	30
NGC7538-IRS9	12.5	74 ± 13	9	31
	20	124 ± 30	6	31
	25	260 ± 50	6	31
	30	500 ± 150	40	31
	50	1300 ± 390	40	31
	100	2700 ± 810	55	31
	350	330 ± 66	120	8
	1000	51 ± 5	55	31
S157	12	29 ± 3	300x45	2
	25	233 ± 12	300x45	2
	60	1759 ± 123	90x300	2
	100	264 ± 303	180x300	2
	350	280 ± 56	120	8
	850	5.9 ± 1.2	18	10

[1]REFERENCES: (1) MSX Database. (2) IRAS PSC 1988. (3) Mottram et al. 2010. (4) AKARI Database. (5) SCUBA Legacy Catalogs. (6) Aguirre et al. 2011. (7) Mookerjea et al. 1999. (8) Mueller et al. 2002. (9) Dent, Matthews, & Ward-Thompson 1998. (10) Jenness, Scott, & Padman 1995. (11) McCutcheon et al. 1995. (12) Chini, Henning, & Pfau 1991. (13) Tothill 1999. (14) Chini et al. 1986a. (15) Fazio et al. 1978. (16) Chini et al. 1986b. (17) Jaffe et al. 1984. (18) Jenness 1996. (19) Evans et al. 1979. (20) Dyck & Simon 1977. (21) Stier 1984. (22) Guertler et al. 1991. (23) Cheung et al. 1980. (24) Soifer & Pipher 1975. (25) Hatchell et al. 2000. (26) Zhou et al. 1994. (27) Ellis et al. 1990. (28) Evans et al. 1981b. (29) Moriarty-Schieven, Snell, & Hughes 1991. (30) Gordon 1990. (31) Werner et al. 1979.

Table 5. Bayesian linear correlations

Line	Set	Variables	Cutoff	b	a	σ_{int}
HCO^+ (3-2)	Galactic	L_{bol}-L′	None	1.10 ± 0.12	3.26 ± 0.16	0.15
HCO^+ (3-2)	Extragalactic	L_{bol}-L′	None	0.81 ± 0.21	5.22 ± 1.68	0.06
HCO^+ (3-2)	Combined	L_{bol}-L′	None	1.04 ± 0.02	3.33 ± 0.07	0.12
HCN (1-0)	Galactic	L_{bol}-L′	None	1.25 ± 0.10	2.47 ± 0.19	0.41
HCN (1-0)	Extragalactic	L_{bol}-L′	None	1.07 ± 0.06	2.32 ± 0.53	0.05
HCN (1-0)	Combined	L_{bol}-L′	None	1.01 ± 0.02	2.82 ± 0.10	0.25
HCN (1-0)	Galactic	L_{bol}-L′	$>10^3$ $L_\odot$	0.92 ± 0.13	3.18 ± 0.27	0.36
HCN (1-0)	Combined	L_{bol}-L′	$>10^3$ $L_\odot$	0.98 ± 0.02	3.08 ± 0.10	0.19
HCN (1-0)	Galactic	L_{bol}-L′	$>10^{4.5}$ $L_\odot$	0.55 ± 0.15	4.19 ± 0.35	0.29
HCN (1-0)	Combined	L_{bol}-L′	$>10^{4.5}$ $L_\odot$	0.94 ± 0.02	3.35 ± 0.11	0.17
HCO^+ (3-2)	BGPS-MSX	L′-M_{iso}	None	0.84 ± 0.17	-1.62 ± 0.56	0.14
HCO^+ (3-2)	H_2O maser	L′-M_{iso}	None	0.85 ± 0.18	-1.82 ± 0.70	0.09
HCO^+ (3-2)	Combined	L′-M_{iso}	None	0.78 ± 0.10	-1.48 ± 0.35	0.08
HCO^+ (3-2)	BGPS-MSX	L′-M_{vir}	None	1.06 ± 0.43	-2.23 ± 1.34	0.32
HCO^+ (3-2)	H_2O maser	L′-M_{vir}	None	1.00 ± 0.20	-1.86 ± 0.63	0.12
HCO^+ (3-2)	Combined	L′-M_{vir}	None	1.06 ± 0.18	-2.13 ± 0.56	0.15

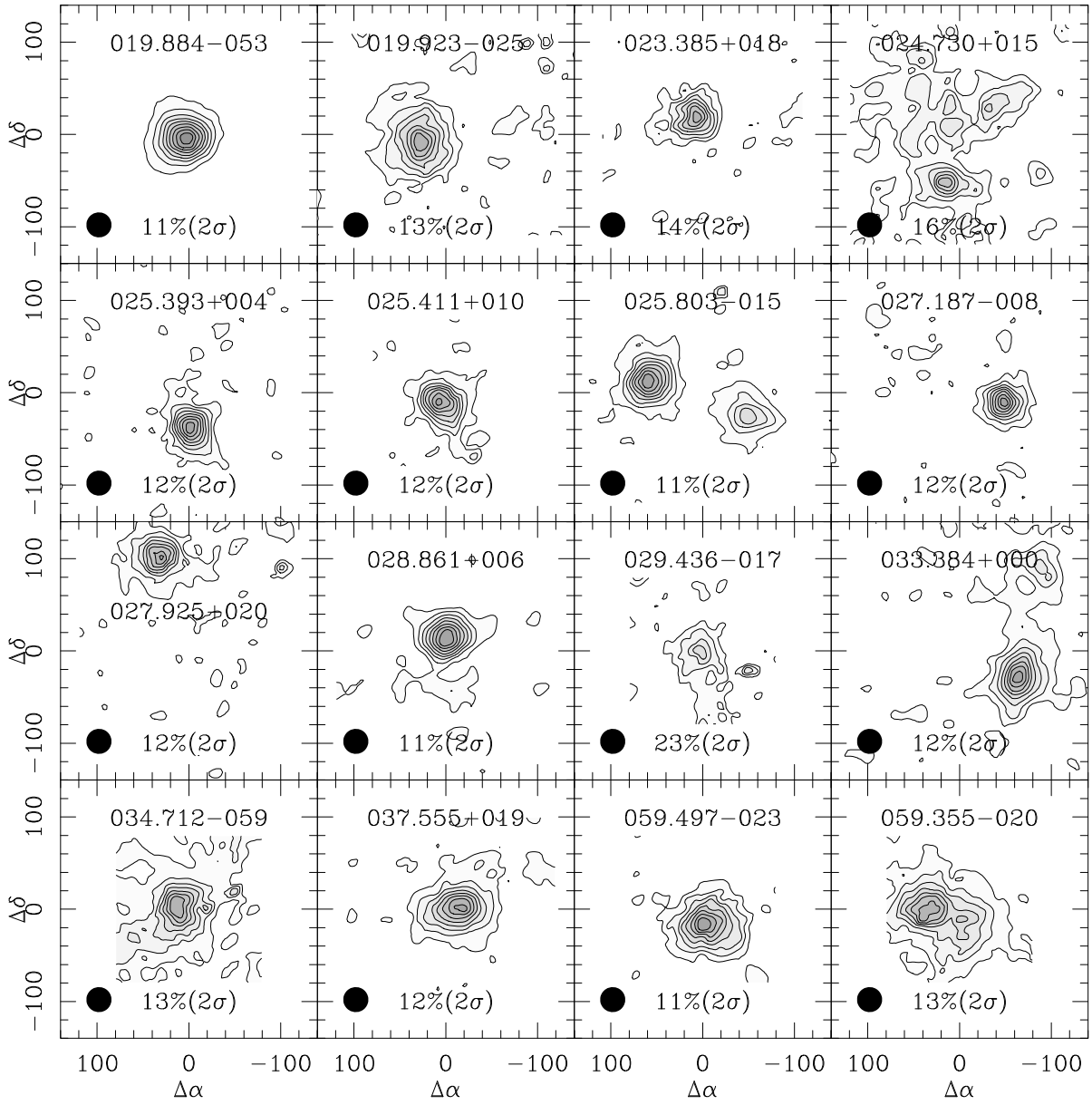

Fig. 1.— HCO^+ (3-2) maps for BGPS/RMS sources. The lowest intensity contour and the contour interval are both 2 σ in each map. The percentage of the 2 σ intensity is also specified.

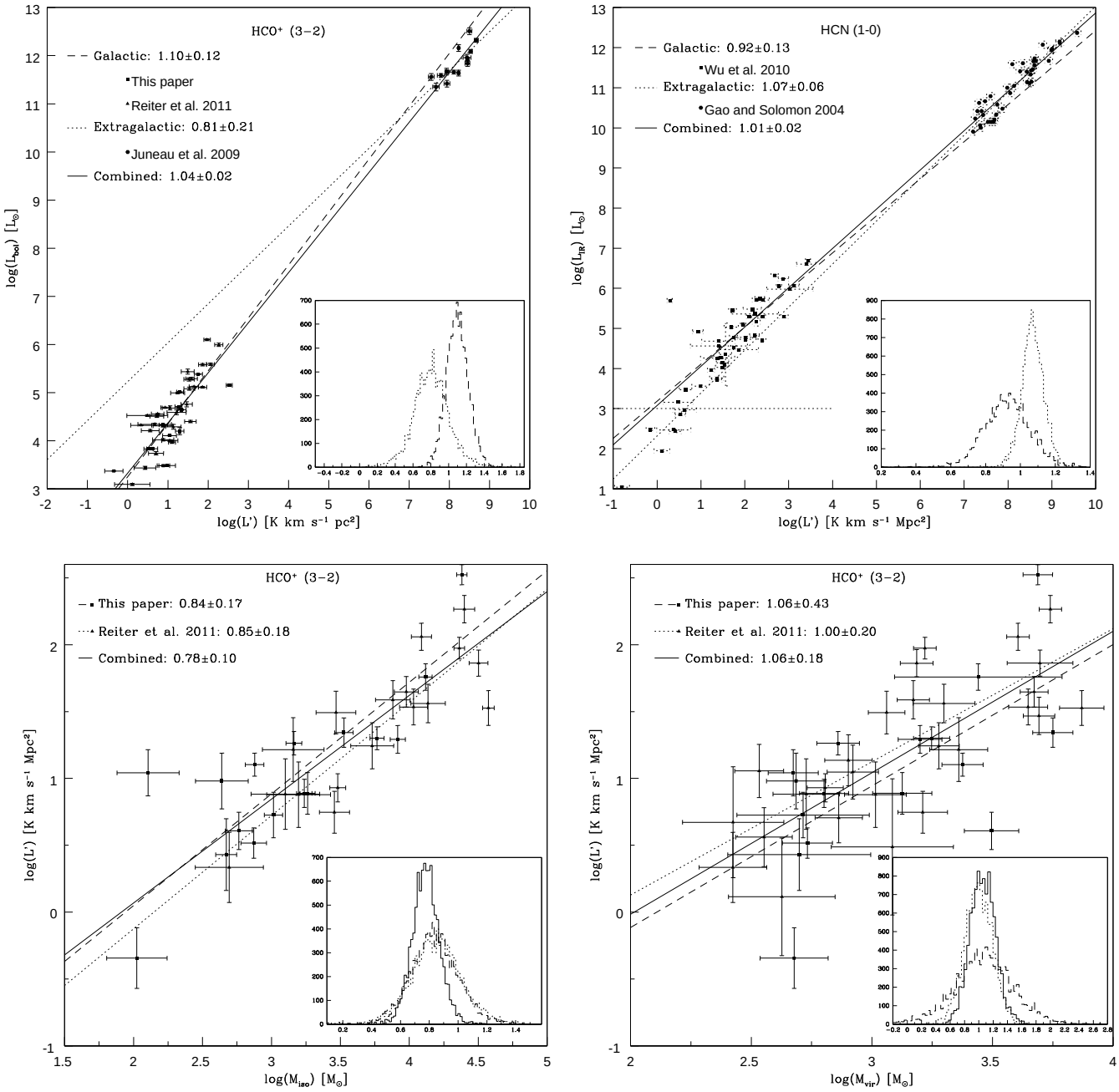

Fig. 2.— Top left: $\log(L_{bol})$-$\log(L')$ for HCO^+ (3-2). Top right: $\log(L_{bol})$-$\log(L')$ for HCN (1-0). Bottom left: $\log(L')$-$\log(M_{iso})$ for HCO^+ (3-2).Bottom right: $\log(L')$-$\log(M_{vir})$ for HCO^+ (3-2).

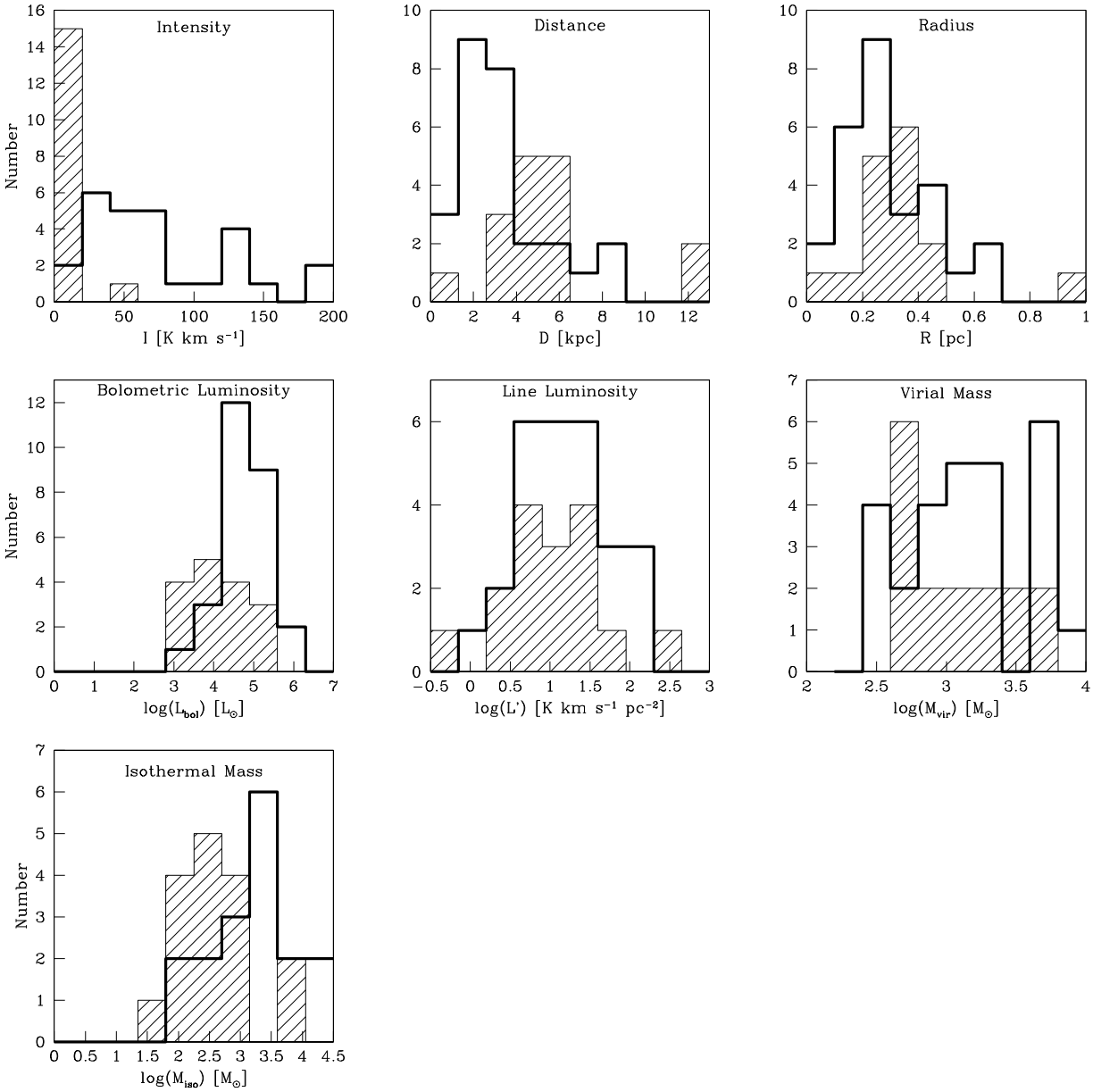

Fig. 3.— Histograms of source properties. The bold line histograms represent the BGPS/RMS sources and the shaded histograms represent the water-maser sources.

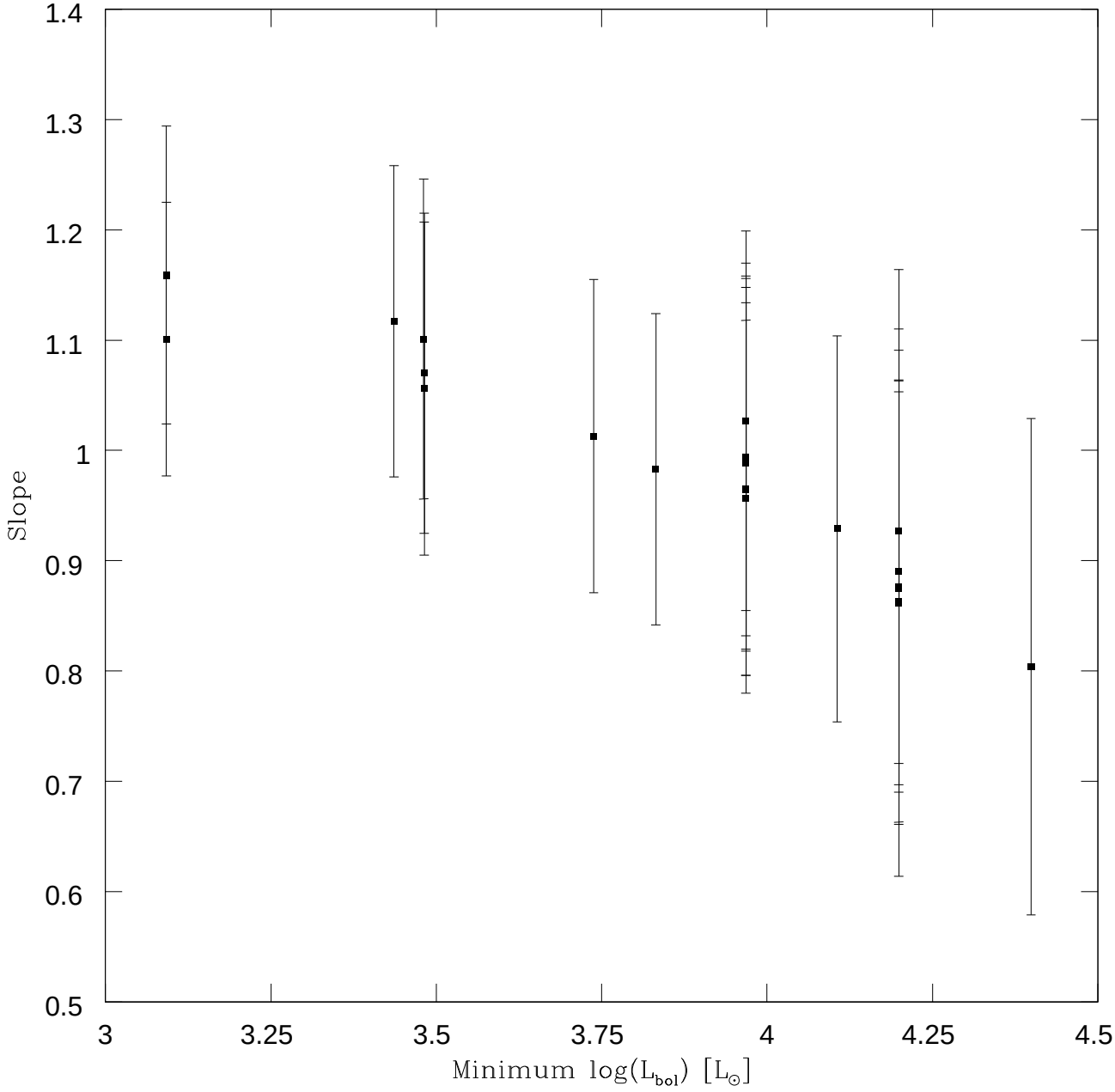

Fig. 4.— The slope of the Bayesian linear fit as a function of the minimum L_{bol}.

The University of Arizona Electronic Theses and Dissertations Reproduction and Distribution Rights Form

Name: Schenck, David Eric

Degree title (eg BA, BS, BSE, BSB, BFA): BS

Honors area: Astronomy

Date thesis submitted to Honors College: May 4, 2011

Title of Honors thesis:
Testing the Global Star Formation Relation: An HCO+ (3-2) Mapping Study of Red MSX Sources in the BOLOCAM Galactic Plane Survey

:The University of Arizona Library Release	I hereby grant to the University of Arizona Library the nonexclusive worldwide right to reproduce and distribute my dissertation or thesis and abstract (herein, the "licensed materials"), in whole or in part, in any and all media of distribution and in any format in existence now or developed in the future. I represent and warrant to the University of Arizona that the licensed materials are my original work, that I am the sole owner of all rights in and to the licensed materials, and that none of the licensed materials infringe or violate the rights of others. I further represent that I have obtained all necessary rights to permit the University of Arizona Library to reproduce and distribute any nonpublic third party software necessary to access, display, run or print my dissertation or thesis. I acknowledge that University of Arizona Library may elect not to distribute my dissertation or thesis in digital format if, in its reasonable judgment, it believes all such rights have not been secured. Signed: David Eric Schenck Date: 5/3/2011

Contributors

Dr. Yancy Shirley (advisor): Provided the original idea for the project and valuable input throughout the process through weekly meetings. He helped organize the observations and was responsible for a large amount of the editing of the paper.

Megan Reiter: Graduate student who supplied data on Galactic clumps mapped in HCO^+ (3-2) and helped explain how to run software she had written. She also provided comments on the paper.

Stephanie Juneau: Graduate student who supplied data and whose 2009 paper was an important resource. She provided comments on the paper.

Timothy-Ellsworth Bowers: Graduate student at the University of Colorado at Boulder who provided results from his PhD. thesis work on distance determination of BGPS sources.

Brandon Kelly: Helped explain how his Bayesian linear regression program operated.

Jingwen Wu: Provided a great deal of data and information from his 2010 paper. He helped explain the contents of the paper necessary for completing the project.